Two Different Pathways toward Convective Self-aggregation in Radiative-convective Equilibrium Simulations between SCALE and VVM

Jin-De Huang[1], Ching-Shu Hung[2], Chien-Ming Wu[1], and Hiroaki Miura[2]

1. Department of Atmospheric Sciences, National Taiwan University, Taipei, Taiwan

2. Department of Earth and Planetary Science, Graduate School of Science, The University of Tokyo, Tokyo, Japan

Corresponding authors: Chien-Ming Wu (mog@as.ntu.edu.tw)

Key points:

- Under the same SST, convective self-aggregation develops differently: gradual transition in SCALE and fast growth in VVM.

- Radiative cooling dominates convective self-aggregation developing in SCALE, while convection efficiently drives the circulation in VVM.

- The different pathways to convective self-aggregation in SCALE and VVM are associated with the transition to large-size convective systems.

20   **Abstract**

21   Two cloud-resolving models (SCALE and VVM) take different pathways toward

22   convective self-aggregation (CSA) in the radiative-convective equilibrium simulations,

23   although they have similar domain-averaged properties. Analyses in the moisture space show

24   that radiative cooling in the dry area mainly drives CSA in SCALE, while subsidence triggered

25   by the convection in the moist region dominates in VVM. The change in the convective

26   structures is found on the isentropic diagram in VVM, but this transition is unclear in SCALE.

27   The object-based analysis provides that the convective systems with larger sizes are rare in

28   SCALE. In contrast, large-size convective systems frequently develop in the moist region as

29   CSA evolves in VVM. The large-size systems can efficiently drive the circulation between the

30   dry and moist areas. The different pathways to CSA are associated with the transition of

31   convective structures, which provides a new insight to understand CSA among cloud-resolving

32   models based on the perspective of the mechanism.

33   **Plain Language Summary**

34   A variety of deep convective clouds is found in the tropics, and they sometimes form

35   clusters. Previous studies have found that the mechanisms for the onset of the clustered

36   convection are very different in warmer and colder sea surface temperature conditions in

37   idealized numerical experiments. We discover that the mechanisms can be different among the

38   two models even though the sea surface temperature is the same. The clustering in one model

39   is driven by the radiative processes in the region without convection. In the other model, the

40   clustering is controlled by circulation from the region with larger convective clouds. This study

41   shows that the different mechanisms for the onset of the clustered convection are related to the

42   structures of convective clouds among models. This result improves our understanding of the

43   clustered convection in the models.

44

1 Introduction

Radiative convective equilibrium (RCE) is known as a conceptual model for understanding tropical climate (Manabe and Strickler, 1964). In this model, moist convection is essential to balance the radiative cooling and the surface warming to reach an equilibrium climate state with a statically stable thermodynamic structure. This concept has been applied using cloud-resolving models (CRMs), and the models reach equilibrium states with smaller convective regions surrounded by larger and wider dry subsiding regions, which is called convective self-aggregation (CSA; Nakajima and Matsuno, 1988; Held et al., 1993; Tompkins and Craig, 1998; Bretherton et al., 2005; Muller and Held, 2012; Wing and Emanuel, 2014; Yanase and Takemi, 2018). CSA changes the energy balance of the atmospheric column and then leads to the impact on climate sensitivity (Mauritsen and Stevens, 2015; Holloway et al., 2017; Wing, 2019). Wing et al. (2018, 2020) organized the RCE Model Intercomparison Project (RCEMIP) to investigate the role of clouds and CSA in the climate sensitivity. Even though CRMs are forced by the same sea surface temperature (SST), large differences in the vertical structures of temperature, humidity, and cloudiness are found across the RCEMIP ensemble of CRMs. These CRMs also exhibit discrepancies in the degree of CSA and its dependency on SST. It is difficult to identify a specific process that causes the spread results in the RCEMIP ensemble because these models are treated with different dynamics and physics.

Coppin and Bony (2015) showed that the leading mechanism for CSA varies with SST using an atmospheric general circulation model. At low SST, the radiative cooling due to low clouds in dry areas drives large-scale subsidence, which is called a radiative-driven cold pool. The expansion of the radiative-driven cold pool forces convection to aggregate in the regions with weak subsidence, and this mechanism mainly contributes to CSA under the cold SST conditions. On the other hand, at high SST, deep convection develops and then induces strong

70 surface wind, which leads to enhanced surface enthalpy flux in the adjacent region. The

71 enhanced surface flux will favor the subsequent development of deep convection in similar

72 areas, and this feedback controls the development of CSA under high SST conditions. The idea

73 of different mechanisms provides a hint that the main process of maintaining CSA could be

74 distinct among CRMs, which causes the different sensitivities to the changing SST in the

75 RCEMIP ensemble.

76

77   This study investigates the crucial mechanism leading to CSA using two CRMs, and

78 the experimental setups follow the RCEMIP protocol (Wing et al., 2018), except for the domain

79 size. The equilibrium state with CSA is obtained in the simulations with a medium domain size

80 to reduce computational cost. We analyze the results in the moisture space to evaluate the

81 differences in the equilibrium state. The isentropic analysis (Pauluis and Mrowiec, 2013) and

82 the object-based analysis method are applied to examine the time evolution of the convective

83 structures as CSA develops. Section 2 describes the two models and the experimental setup.

84 Section 3 presents the differences in the equilibrium states, the mechanism for CSA, and the

85 convective structures between two CRMs. The summary and discussion are in section 4.

86

87   **2   Models and Experiment Design**

88   2.1 Model description

89   2.2.1 SCALE

90   The first atmospheric model used in this study is a regional model constructed with

91   Scalable Computing for Advanced Library and Environment (SCALE, Version 5.3.6;

92   Nishizawa et al., 2015; Sato et al., 2015). The model is governed by the three-dimensional fully

93   compressible non-hydrostatic equations, which predicts the three-dimensional momentum (ρu,

94   ρv, and ρw), total density (ρ), mass-weighted potential temperature ($\rho\theta$), and mass

95   concentration of tracers (ρq_s). The θ here is not the conventional potential temperature for dry

96   air, but the corresponding value for total air, considering water content. A six-class single-

97   moment bulk-type microphysics scheme is used in this study (Tomita, 2008). The subgrid-scale

98   turbulent process is parameterized through the Smagorinsky-Lilly type first-order closure

99   scheme (Brown et al., 1994; Scotti et al., 1993), and surface fluxes are calculated by a bulk

100   method using a universal function (Beljaars and Holtslag, 1991; Wilson, 2001). The radiative

101   processes are treated with a k-distribution-based broadband radiation transfer model (Mstrn-X,

102   Sekiguchi and Nakajima, 2008). SCALE has been used in studying the impacts of cloud

103   microphysics on convection (Sato et al., 2015, 2018), data assimilation (Honda et al., 2018,

104   2019), regional climate changes (Adachi et al., 2019), severe weather events (Yoshida et al.,

105   2019), the parameterization of physical processes (Iwabuchi and Okamura, 2017; Nishizawa

106   et al., 2018), and dynamical downscaling of blowing snow events (Tanji et al., 2019; Inatsu et

107   al., 2020).

108

109   2.2.2 VVM

110   The other model used in this study is the vector vorticity equation cloud-resolving

111   model (VVM) developed by Jung and Arakawa (2008). Horizontal components of anelastic

112   vorticity equations are predicted in the VVM, and velocities are diagnosed through solving a

113   three-dimensional elliptic equation. The use of the vorticity equations eliminates pressure

114   gradient force and inherently links the dynamics and the thermodynamics in the governing

115   equations. The direct couple in the equations can better capture local circulations associated

116   with strong thermal gradients, such as the land-sea breeze. Radiative fluxes are calculated by a

117   radiative transfer model using the correlated-k approach (Iacono et al., 2008), surface fluxes

118   are treated by the Monin-Obukhov similarity theory (Chen and Dudhia, 2001), microphysical

119   processes are parameterized by the two-moment bulk scheme that predicts properties of ice

120   particles (Morrison and Milbrandt, 2015; Huang and Wu, 2020), and the effects of the

121   topography are represented by the immersed boundary method in the VVM (Wu and Arakawa,

122   2011; Chien and Wu, 2016). VVM has been applied in many studies, such as unified

123   parameterization (Arakawa and Wu, 2013; Wu and Arakawa, 2014), stratocumulus dynamics

124   (Tsai and Wu, 2016), afternoon thunderstorms (Kuo and Wu, 2019), impacts of land surface

125   heterogeneity (Wu et al., 2019; Wu and Chen, 2021), cloud-aerosol interactions (Chang et al.,

126   2021), coastal convection during summer monsoon onset (Chen et al., 2019), and the

127   aggregated convection (Tsai and Wu, 2017; Chen and Wu, 2019).

128

129   2.2 Experiment design

130   VVM and SCALE used their own default physics settings with the same experimental

131   settings, such as solar insolation and greenhouse gas profiles, following the RCEMIP protocol

132   (Wing et al., 2018). The simulations are initialized from an analytically approximated sounding

133   of the moist tropics (Dunion, 2011) and integrated with a fixed SST of 300 K for 50 days with

134   hourly data outputs. Yanase et al. (2020) investigated and suggested that 384 km is the

135   minimum size for CSA in SCALE with the 2-km resolution. The domain size of 384×384 km^2

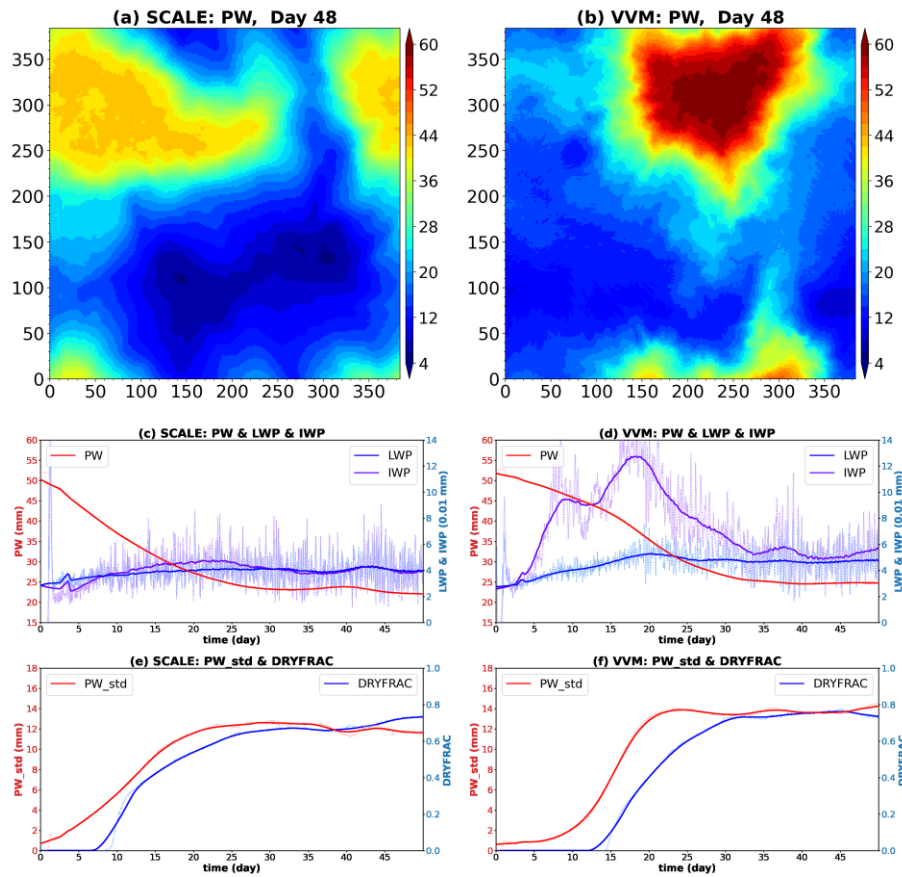136   with a 2-km horizontal resolution is used to have minimal costs for CSA.

137

138   3   Result

Fig. 1. The horizontal distribution of daily averaged PW on day 48 for SCALE (a) and VVM (b). The time evolutions of domain-averaged precipitable water (PW), liquid water path (LWP), and ice water path (IWP) for SCALE (c) and VVM (d). The time series of the standard deviation of PW (PW_std) and the dry area fraction (DRYFRAC) for SCALE (e) and VVM (f). The solid lines represent the 5-day moving averages of each variable, and the dashed lines are shown without the temporal smoothing.

139   3.1 Overall behaviors of two models

140   The occurrence of CSA can be visualized by the spatial distribution of daily averaged

141   precipitable water (PW) on day 48 in SCALE (Fig. 1a) and VVM (Fig. 1b). A clear structure

142   that a moist region surrounded by the dry area can be seen in both models. PW in the moist

143   region reaches 56 mm in VVM, which is significantly greater than that in SCALE (42 mm).

144   PW in both models is similar in the dry areas, but PW in some small regions is less than 10

145   mm in SCALE. We used several variables to quantify the differences in the evolutions of CSA

146   (Fig. 1c and 1d). The domain average of PW declines as the time proceeds in both models, and

147   they reach a quasi-steady state after day 40 with the mean PW of 25 mm. Throughout the

148   transition toward CSA, the liquid water path (LWP) similarly evolves in both models, but the

149   evolution of the ice water path (IWP) is different between SCALE and VVM. IWP in VVM

150   significantly increases before day 20 and then settles to equilibrium, while a smaller temporal

151   variation of IWP is found in SCALE. The difference in IWP suggests that VVM undergoes a

152   drastic transition of cloud structures during the development of CSA.

153

154   We apply the dry fraction and the standard deviation of PW to identify the differences

155   in the degree of CSA between SCALE and VVM (Fig. 1e and 1f). The dry fraction (DRYFRAC)

156   is defined as the fraction of areas where precipitable water is lower than 30 mm (Yanase et al.

157   2020). DRYFRAC of SCALE starts its increase at day 8, while DRYFRAC of VVM starts

158   increasing at day 13. DRYFRAC in both models reaches 0.7 in the quasi-equilibrium states.

159   DRYFRAC in SCALE gradually grows from 0.6 at day 25 to 0.7 at day 44, while it in VVM

160   reaches 0.7 at day 30 and remains a quasi-steady state. On the other hand, the standard deviation

161   of PW (PW_{std}) shows evident differences in the degree of CSA in both the developing stage

162   and quasi-equilibrium state. In SCALE, PW_{std} linearly increases before day 20 and then

163   remains the quasi-equilibrium state with 12 mm PW_{std}. In VVM, PW_{std} exponentially grows

164   in the first twenty days, and the sharp growth in days 10-20 accompanies the significant change

165   in IWP. In the quasi-equilibrium state, PW_{std} of VVM is 2 mm greater than that of SCALE,

166   which suggests that CSA in VVM would be more aggregated. These results show that the

167   development of CSA is gradual in SCALE, while the quick transition in VVM could be related

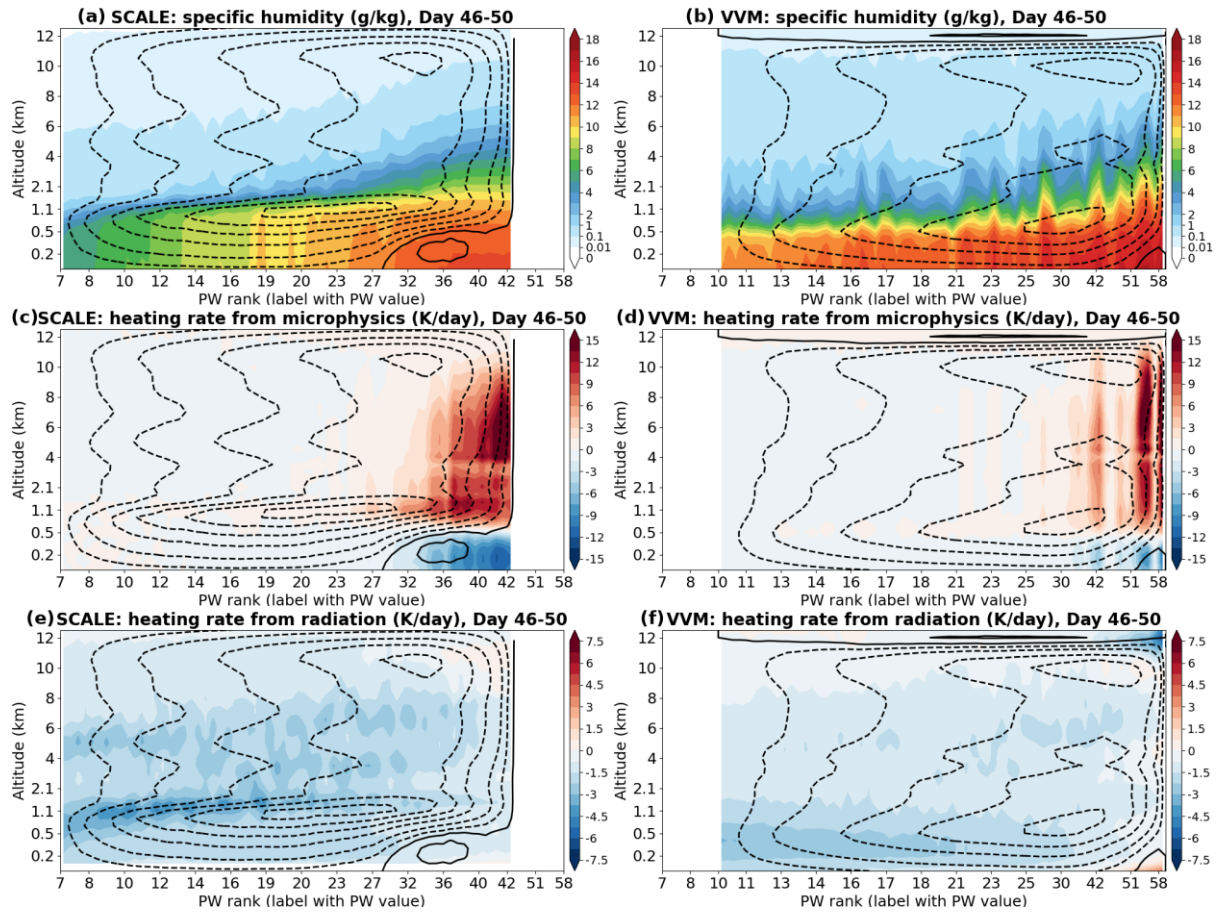168   to the drastic changes in the cloud structures.

Fig. 2. The vertical profiles of specific humidity (a, b), microphysical latent heating rate (c, d), radiative heating rate (e, f) are ranked by precipitable water with the same sample size in each rank for SCALE (left) and VVM (right) in days 46-50 (Note that the PW range is different for SCALE and VVM). Contours show the streamfunction with intervals of 0.05 kg m^{-2} s^{-1}, and the contours of -0.02 and 0.02 kg m^{-2} s^{-1} are added to show subsidence in the drier region and clockwise circulation in the moister region, respectively. The solid and dash lines, respectively, represent clockwise and counterclockwise circulations in the moisture space.

170   3.2 CSA in the moisture space

171   The characteristics of CSA in the quasi-equilibrium state are evaluated by the vertical

172   profiles ranked by PW following Bretherton et al. (2005). Fig 2a and 2b show that

173   counterclockwise circulations in the moisture space are evident in both models with a narrower

174   upward branch in the moister region (over 36 mm for SCALE and over 51 mm for VVM) and

175   wider subsidence in the drier region (7-23 mm in SCALE and 10-25 mm for VVM). The overall

176   range of PW in VVM is moister compared to that in SCALE. Even though atmospheric

177   columns have the same PW in the two models, the values of water vapor mixing ratio in both

178   boundary layer and free atmosphere are smaller in SCALE. Another notable difference in the

179   circulations in the dry areas is that the counterclockwise circulations of SCALE are stronger

180   and have a gap at the top of the boundary layer, while the boundary layer circulation of VVM

181   is weaker and more smoothly connected with the free-atmospheric circulation. Besides, the

182   ascending branch of the circulation is confined in the moister 10 % region in VVM, while that

183   in SCALE has a wider upward motion region in the moisture space. The moisture space

184   analyses show that the structures of moisture and circulation are quite different even though

185   CSA occurs with similar domain-averaged quantities.

186

187   We compare the latent and radiative heating to investigate the mechanisms for the

188   different characteristics of CSA observed in the moisture space. In both models, the condensate

189   heating is consistent with their ascending branch of the circulation in the moisture space (Fig.

190   2c and 2d). There are large differences in the dry areas between the two models. Fig. 2e and 2f

191   show that the radiative cooling in the dry areas is generally stronger in the free atmosphere in

192   SCALE. The sharp transition of the circulation at the boundary layer top in SCALE

193   corresponds to the most significant radiative cooling (Fig. 2e). The results suggest that the

194   mechanism for CSA in SCALE is similar to the radiative-driven cool pool mechanism proposed

195   by Coppin and Bony (2015). The mechanism describes that the radiative cooling due to low

196   clouds in the dry areas drives low-level circulations, and convection is then pushed by the

197   circulation to the humid areas. The low-cloud in their study plays a critical role in the radiation-

198   circulation interaction. In our study, the features of the stronger radiative cooling and enhanced

199   low-level circulation are found in SCALE, but there is no low cloud developing in the dry

200   region. We attribute the strong radiative cooling to the drier free atmosphere in SCALE. The

201   drier environment reduces the emissivity of the free atmosphere and leads to efficient cooling

202   at the boundary layer top, which can drive shallow circulation as low clouds. Besides, the drier

203   environment in SCALE enhances the evaporation of rain water, so the boundary layer in the

204   moist region has significant cooling signals in SCALE (Fig. 2c). The mechanism for CSA in

205   SCALE is close to the leading mechanism under the cold mean states in Coppin and Bony

206   (2015), but it is due to a drier environment rather than the low clouds in the dry areas.

207

208   The features of VVM in the moisture space provide a possible mechanism for CSA.

209   The ascending branch is confined in the region where PW greater than 51 mm accompanying

210   with considerable microphysical heating (Fig. 2d). The radiative cooling in VVM is weaker

211   compared to SCALE (Fig. 2e and 2f). CSA is mainly driven by the convection in the narrow

212   moist areas in VVM, which indicates that the condensate heating is more efficient in driving

213   circulation (Hack and Schubert 1986). The mechanism for CSA in VVM would be similar to

214   the wind-induced surface heat exchange (WISHE) mechanism under the warm mean states in

215   Coppin and Bony (2015). The circulations triggered by convection enhance the surface wind

216   and turbulent enthalpy flux, and it can lead to the convergence of heat in the convective region

217   from the far region. These responses favor the subsequent development of convection in the

218   adjacent areas of existing convection. This mechanism is consistent with that CSA is controlled

219   by convection in VVM. Besides, the more humid PW range and boundary layer in VVM could

220   be attributed to the enhanced surface enthalpy flux. Although the two models are forced by the

221   same SST, the analyses in the moisture space clarify that different mechanisms for CSA are the

222   radiative-driven cool pool feedback in SCALE and the WISHE feedback in VVM.
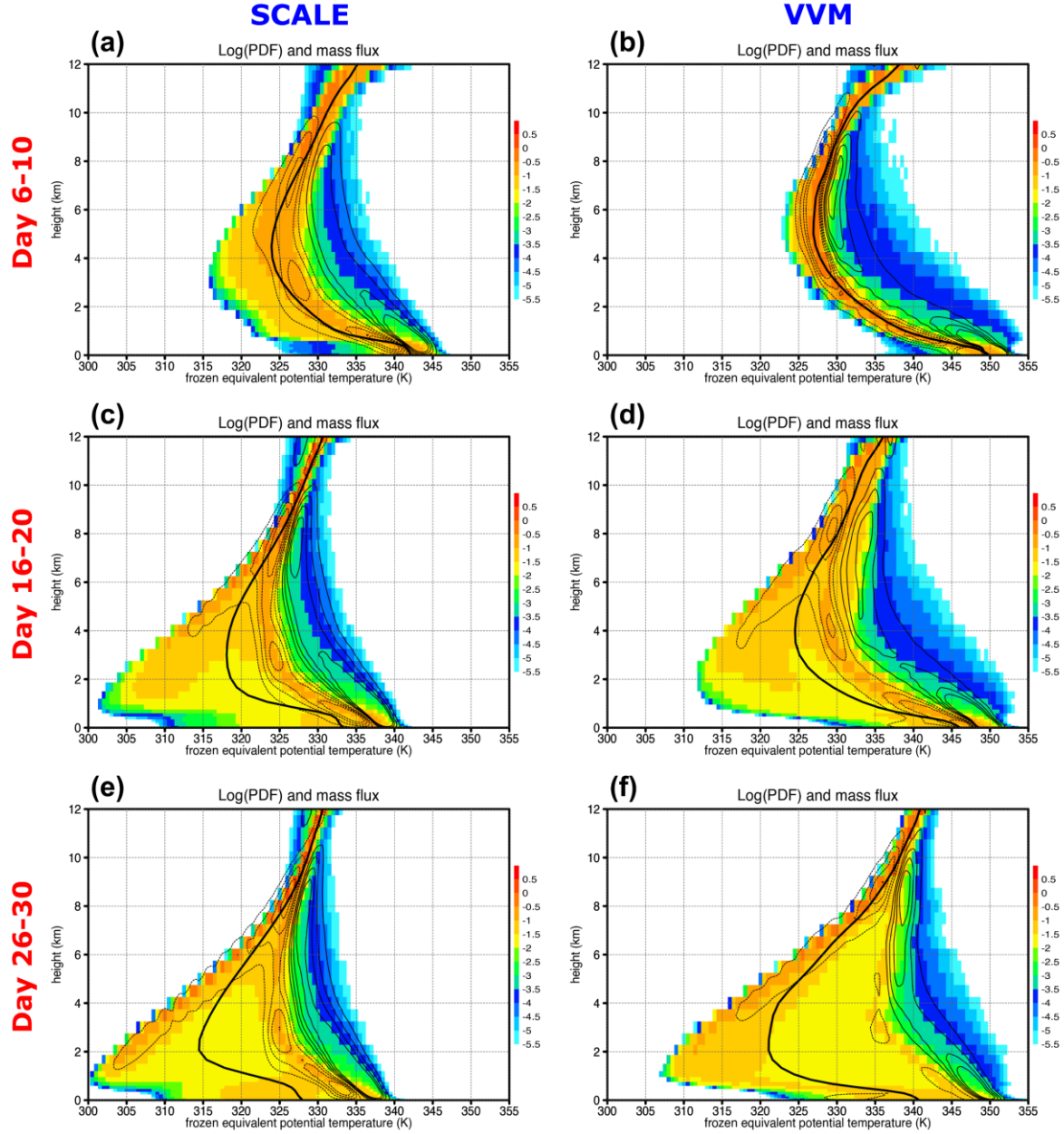
223

Fig. 3. The isentropic analysis of SCALE (left panels) and VVM (right panels) for days 6-10 (a, b), days 16-20 (c, d), and days 26-30 (e, f). The solid black line represents the mean frozen equivalent potential temperature (θ_{ei}) and the color shading represents the logarithmic probability density function of θ_{ei}. The isentropic mass fluxes are presented by the contours with the interval of 0.003 kg m^{-2} K^{-1}.

225   3.3 Isentropic analyses on the evolution of CSA

226   During the developing stage of CSA, the drastic changes in the temporal evolution of

227   IWP in VVM hints on the transitions of cloud structures. The different mechanism for CSA in

228   SCALE and VVM could be related to the cloud structure changes. We apply the isentropic

229   analysis (Pauluis and Mrowiec, 2013) to investigate the convective structures via the energetic

230   perspective (Huang and Wu 2020). The isentropic distribution is calculated through conditional

231   sampling by the air parcel's frozen equivalent potential temperature (θ_{ei}) following Pauluis

232   (2016). The isentropic mass fluxes could be approximated as the convective parcels'

233   trajectories on the energy space. The isentropic analysis is applied to days 6-10 (Fig. 3a and

234   3b), days 16-20 (Fig. 3c and 3d), and days 26-30 (Fig. 3e and 3f) for both models to focus on

235   the changes in the developing stage of CSA.

236

237   In days 6-10, the isentropic distributions are single-peak with maximum occurrences

238   around the mean θ_{ei} profile. The subsiding mass fluxes associated with the high occurrences

239   indicate that the subsidence occurs in vast areas, and convection develops in the limited areas.

240   SCALE has wider isentropic distributions for the altitudes between 1 km and 8 km during days

241   6-10 because dry areas start to expand (Fig. 3a). In VVM, CSA does not develop yet, so

242   isentropic distributions are concentrated and close to the domain-averaged θ_{ei} profile (Fig. 3b).

243   Both models have a local maximum of upward and downward isentropic mass fluxes below 2

244   km height due to the boundary layer mixing. In SCALE, the updraft extends from 2 km to 8

245   km with 5 K changes in θ_{ei}, which indicates the influence of the entrainment, especially in

246   low-levels. The impacts of entrainment are greater in VVM because of the changes of θ_{ei} (10

247   K) along with upward mass fluxes from 2 km to 4 km. Above the freezing level (5 km), the

248   updraft remains at constant with the increase of height.

249

250   During days 16-20, SCALE and VVM share some similarities on the isentropic

251   diagrams (Fig. 3c and 3d). The domain-averaged θ_{ei} profiles shift to lower θ_{ei} region, and the

252   isentropic distributions become bimodal in both models compared to day 6-10. One peak

253   locates at low θ_{ei} region smaller than averaged θ_{ei}, and the other peak remains at the high θ_{ei}

254   region. These features in the isentropic diagrams indicate that CSA develops and leads to the

255   expansion of the dry areas, and the two peaks at high and low θ_{ei} can, respectively, represent

256   the moist and dry regions. An extra subsiding branch of mass flux develops along with the peak

257   at low θ_{ei} in the layer between 4 km and 6 km. The upward mass fluxes become stronger in

258   the moist region compared to days 6-10. These similar features in both models reflect the

259   development of CSA, and these changes from days 6-10 to days 16-20 become more significant

260   as CSA continue developing in days 26-30.

261

262   Notable differences can be seen in the evolutions of the isentropic distributions as CSA

263   develops. The first one is that the overall isentropic distribution in SCALE shifts toward the

264   low θ_{ei} region (surface θ_{ei} is 345 K in days 6-10 and 337 K in days 26-30). In VVM, the peak

265   at low θ_{ei} shifts only, and the peak at high θ_{ei} remains at similar values of θ_{ei} (surface θ_{ei} is

266   350 K). The drier range of PW in the moisture space during the quasi-equilibrium state is highly

267   related to the shift in SCALE. The result suggests that SCALE and VVM undergo different

268   pathways to CSA and finally reach quasi-equilibrium states driven by distinct mechanisms. A

269   hypothesis for the different pathways in SCALE and VVM is provided based on the differences

270   in the evolutions of isentropic mass fluxes in the high θ_{ei} regions. The upward mass fluxes

271   considerably strengthen without large changes in its vertical structure in SCALE. In VVM, the

272   strength of ascending mass fluxes moderately enhances, and its structure becomes steeper in

273   days 26-30 (Fig. 3e) compared to days 6-10 (Fig. 3a). The steeper structure indicates that the

274   effects of the entrainment are reduced. The results suggest that convective structures change as

275   CSA develops in VVM. The convection then becomes more efficient in driving circulations

276   between dry and moist regions even with less upward transports compared to SCALE in days

277   26-30 (Fig. 3e and 3f). The stronger ascending transports is need to keep developing CSA in

278   SCALE. The downward mass fluxes nearby the ascending ones on the isentropic diagram (Fig.

279   3e) indicate that the compensating subsidence occurs in adjacent regions of existing convection

280   in physical space. The subsidence in the moist region causes the lower efficiency in driving the

281   circulations and the suppression of accumulating PW in atmospheric columns. The transition

282   of the convective structures is hypothesized to be critical for the different pathways to CSA in
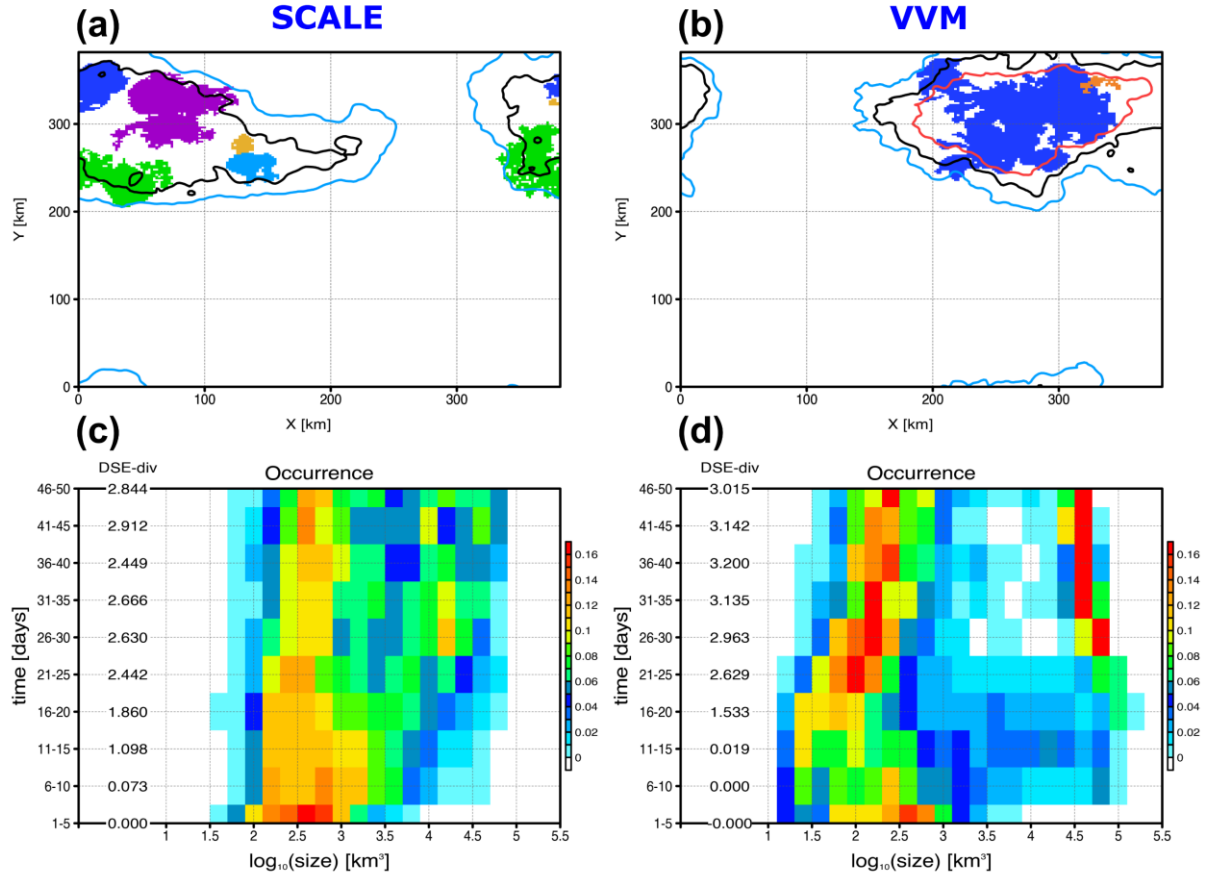
283   SCALE and VVM.

284

Fig. 4. The surface projections of convective cloud on day 48 for SCALE (a) and VVM (b). Precipitable water of 30, 40, and 50 mm are presented by the cyan, black, and red contours, respectively. Time evolutions of cloud size distribution for SCALE (c) and VVM (d) are shown by the color shading with 5-day intervals. The values with the unit of 10^6 J m^{-2} s^{-1} at the left part of the panels present the temporal averages of column flux divergence of dry static energy (DSE-div) in the moist region where PW is greater than 30 mm.

285   3.4 The statistics of convective structure changes

286   We apply the object-based analysis method to investigate the transition of convective

287   structures. This method has been used to study the changes in the convective structure among

288   different environments (Tsai and Wu, 2017; Su et al., 2019). The definition of cloud objects in

289   this study follows Wu and Chen (2021). Contiguous cloudy grids where the total cloud

290   condensates are greater than 10^{-5} kg kg^{-1} are connected and then identified as a convective

291   cloud object using the six-connected segmentation method. Here, we add a condition that the

292   cloud object base is lower than 2 km to ensure convective clouds develop from the boundary

293   layer. Additionally, a criterion that the cloud top height greater than 6 km is used to select the

294   deep convection, which can largely influence the environment and the circulation. The features

295   of convective cloud objects are projected to the surface at day 48 (Fig. 4a and 4b).

296

297   Both models have a similar coverage of the moist area where precipitable water is

298   greater than 30 mm, but the horizontal scales of the convective cloud objects are quite different

299   between SCALE and VVM. Convective cloud objects in SCALE scatter within the moist area

300   with a smaller size. In VVM, the largest cloud object almost occupies the moist area, and some

301   smaller cloud objects surround the largest one. The moist area of VVM is more humid than that

302   of SCALE, and it would support the development of larger convective clouds. The evolution

303   of the size distribution shows that the size of convective clouds tends to be smaller than 10^3

304   km^3 in both models. As CSA develops, the size distributions in both models become a bimodal

305   distribution with peaks of smaller and larger sizes, and the bimodal distribution in VVM is

306   more obvious than that in SCALE. The large-size peak splits from the small-size peak in days

307   6-30 and shifts to about 10^4 km^3 gently in SCALE, while the large-size peak in VVM leaps to

308    $10^{4.5}$ km^3 in days 11-25. The convective cloud objects with a size greater than 10^4 km^3 rarely

309   appear in SCALE, while they frequently develop with larger sizes in VVM. The results suggest

310   that the convective systems in VVM become more organized during the development of CSA.

311

312   The organized convective clouds mostly covering the moist region in VVM can more

313   efficiently drive the circulations between dry and moist regions. In contrast, the smaller

314   convective clouds in SCALE lead to the subsidence in the clear-sky region between the systems,

315 which corresponds to the subsidence nearby the upward motion on the isentropic diagram. That

316 the organized convection can efficiently drive circulations is supported by the divergence of

317 column-integrated dry static energy (DSE-div) in the moist region where PW larger than 30

318 mm. DSE-div in both models increases with the emerge of the large-size peak in the size

319 spectrum. The increase of DSE-div accompanies by the gentle shift of the large-size peak in

320 SCALE, while DSE-div rapidly grows in days 11-25 in VVM when the size distribution sharply

321 transits. After day 30, the exports of DSE in the moist region are greater in VVM, and the

322 greater exports accompany with the larger convective clouds frequently develop. The results

323 confirm that the transition of convection to more organized systems in VVM enhances the

324 efficiency in driving circulations, while the convection without the structure changes is

325 inefficient in SCALE. The discrepancy in the organized structures leads to the different

326 pathways to CSA.

327

4 Summary and Discussion

In this study, RCE simulations are conducted using two CRMs (SCALE and VVM) following the RCEMIP protocol (Wing et al. 2020), and the setups of the horizontal domain and resolution are adopted from Yanase et al. (2020). Our results show that two models undergo two different pathways to CSA even though the two models reach CSA after 40 days. The analyses in the moisture space indicate that CSA in SCALE develops through the strong shallow circulation induced by the enhanced radiative cooling near the boundary layer top. The isentropic and object-based analyses provide evidence that the convective systems in VVM become more organized and then enhance the circulation between the dry and moist regions. The pathways to CSA in SCALE and VVM are, respectively, similar to the mechanisms in cold and warm SST scenarios in Coppin and Bony (2015). In their study, the critical mechanism for the development of CSA varies among SST. Our study highlights that even though CSA in both models is driven by the same SST of 300 K, the critical mechanism for CSA is different between SCALE and VVM.

The different pathways to CSA between SCALE and VVM provide a process-based perspective to understand the diverse results in the RCEMIP ensemble. The different mechanisms also imply different climate sensitivities among models. In SCALE, the development of CSA is driven by radiative cooling, which could largely change the radiative energy budget. The enhanced longwave cooling in the dry areas can offset the warming due to the imbalance of radiative forcing such as the greenhouse gases. As radiative cooling dominates the development of CSA, the climate sensitivity would be smaller in SCALE. On the other hand, CSA develops with the transition of convective structures like VVM. The response of radiation would be inefficient, which leads to larger climate sensitivity. The difference in outgoing longwave radiation is 15 W m^{-2} between SCALE and VVM in the quasi-equilibrium

353   state. It is worth further investigating how the different mechanisms for CSA lead to the spread

354   of CRMs in the RCEMIP ensemble.

355

366

367 **References**

368 Arakawa, A., & Wu, C.-M. (2013). A unified representation of deep moist convection in

369   numerical modeling of the atmosphere. Part I. Journal of the Atmospheric Sciences,

370   70(7), 1977–1992. https://doi.org/10.1175/JAS-D-12-0330.1

371 Beljaars, A. C. M., & Holtslag, A. A. M. (1991). Flux parameterization over land surfaces for

372   atmospheric models. Journal of Applied Meteorology, 30(3), 327–341.

373   https://doi.org/10.1175/1520-0450(1991)030<0327:FPOLSF>2.0.CO;2

374 Bretherton, C. S., Blossey, P. N., & Khairoutdinov, M. (2005). An energy-balance analysis of

375   deep convective self-aggregation above uniform SST. Journal of the Atmospheric

376   Sciences, 62, 4273–4292. https://doi.org/10.1175/JAS3614.1

377 Brown, A. R., Derbyshire, S. H., & Mason, P. J. (1994). Large-eddy simulation of stable

378   atmospheric boundary layers with a revised stochastic subgrid model. Quarterly Journal

379   of the Royal Meteorological Society, 120(520), 1485–1512.

380   https://doi.org/10.1002/qj.49712052004

381 Chang, Y.-H., Chen, W.-T., Wu, C.-M., Moseley, C., & Wu, C.-C. (2021). Tracking the

382   influence of cloud condensation nuclei on summer diurnal precipitating systems over

383   complex topography in Taiwan. Atmospheric Chemistry and Physics. Discuss.

384   https://doi.org/10.5194/acp-2021-113

385 Chen, F., & Dudhia, J. (2001). Coupling an Advanced Land Surface–Hydrology Model with

386   the Penn State–NCAR MM5 Modeling System. Part I: Model Implementation and

387   Sensitivity. Monthly Weather Review, 129(4), 569-585. https://doi.org/10.1175/1520-

388   0493(2001)129<0569:CAALSH>2.0.CO;2

389 Chen, Y.-T., & Wu, C.-M. (2019). The role of interactive SST in the cloud-resolving

390   simulations of aggregated convection. Journal of Advances in Modeling Earth Systems,

391   11, 3321–3340. https://doi.org/10.1029/2019MS001762

392   Chen, W.-T., Wu, C.-M., Tsai, W.-M., Chen, P.-J., & Chen, P.-Y. (2019). Role of coastal

393   convection to moisture buildup during the South China Sea summer monsoon onset.

394   Journal   of   the   Meteorological   Society   of   Japan,   97(6),   1155-1171.

395   https://doi.org/10.2151/jmsj.2019-065

396   Chien, M.-H., & Wu, C.-M. (2016). Representation of topography by partial steps using the

397   immersed boundary method in a vector vorticity equation model (VVM). Journal of

398   Advances   in   Modeling   Earth   Systems,   8,   212–223.

399   https://doi.org/10.1002/2015MS000514

400   Coppin, D., & Bony, S. (2015). Physical mechanisms controlling the initiation of convective

401   self-aggregation in a General Circulation Model. Journal of Advances in Modeling

402   Earth Systems, 7, 2060–2078. https://doi.org/10.1002/2015MS000571

403   Dunion, J. P. (2011). Rewriting the Climatology of the Tropical North Atlantic and Caribbean

404   Sea   Atmosphere,   Journal   of   Climate,   24(3),   893-908.

405   https://doi.org/10.1175/2010JCLI3496.1

406   Held, M. I., Hemler, R. S., & Ramaswamy, V. (1993). Radiative-convective equilibrium with

407   explicit two-dimensional moist convection. Journal of the Atmospheric Sciences, 50,

408   3909–3927.   https://doi.org/10.1175/1520-

409   0469(1993)050%3C3909:RCEWET%3E2.0.CO;2

410   Holloway, C. E., Wing, A. A., & Bony, S., et al. (2017). Observing Convective Aggregation.

411   Surveys in Geophysics, 38, 1199–1236. https://doi.org/10.1007/s10712-017-9419-1

412   Honda, T., Kotsuki, S., Lien, G.-Y., Maejima, Y., Okamoto, K. & Miyoshi, T. (2018).

413   Assimilation of Himawari-8 all-sky radiances every 10 minutes: Impact on

414   precipitation and flood risk prediction. Journal of Geophysical Research: Atmospheres,

415   123, 965– 976. https://doi.org/10.1002/2017JD027096

416 Honda, T., Takino, S., & Miyoshi, T. (2019). Improving a precipitation forecast by assimilating

417   all-sky himawari-8 satellite radiances: A case of Typhoon Malakas (2016). Scientific

418   Online Letters on the Atmosphere, 15, 7–11. https://doi.org/10.2151/sola.2019-002

419 Huang, J.-D., & Wu, C.-M. (2020). Effects of microphysical processes on the precipitation

420   Spectrum in a strongly forced environment. Earth and Space Science, 7,

421   e2020EA001190. https://doi.org/10.1029/2020EA001190

422 Iacono, M. J., Delamere, J. S., Mlawer, E. J., Shephard, M. W., Clough, S. A., & Collins, W.

423   D. (2008), Radiative forcing by long-lived greenhouse gases: Calculations with the

424   AER radiative transfer models. Journal of Geophysical Research: Atmospheres, 113,

425   D13103. https://doi.org/10.1029/2008JD009944

426 Inatsu, M., Tanji, S., & Sato, Y. (2020). Toward predicting expressway closures due to blowing

427   snow events. Cold Regions Science and Technology, 177, 103123.

428   https://doi.org/10.1016/j.coldregions.2020.103123.

429 Iwabuchi, H., & Okamura, R. (2017). Multispectral Monte Carlo radiative transfer simulation

430   by the maximum cross-section method. Journal of Quantitative Spectroscopy and

431   Radiative Transfer, 193, 40-46. https://doi.org/10.1016/j.jqsrt.2017.01.025.

432 Jung, J.-H., & Arakawa, A. (2008). A three-dimensional anelastic model based on the vorticity

433   equation. Monthly Weather Review., 136(1), 276–294.

434   https://doi.org/10.1175/2007MWR2095.1

435 Kuo, K.-T., & Wu, C.-M. (2019). The precipitation hotspots of afternoon thunderstorms over

436   the Taipei Basin: Idealized numerical simulations. Journal of the Meteorological

437   Society of Japan, 97(2), 501–517. https://doi.org/10.2151/jmsj.2019-031

438   Manabe, S., & Strickler, R. F. (1964). Thermal Equilibrium of the Atmosphere with a

439   Convective Adjustment, Journal of Atmospheric Sciences, 21(4), 361-385.

440   https://doi.org/10.1175/1520-0469(1964)021<0361:TEOTAW>2.0.CO;2

441   Mauritsen, T., & Stevens, B. (2015). Missing iris effect as a possible cause of muted

442   hydrological change and high climate sensitivity in models. Nature Geoscience, 8, 346–

443   351. https://doi.org/10.1038/ngeo2414

444   Morrison, H., & Milbrandt, J. A. (2015). Parameterization of ice microphysics based on the

445   prediction of bulk particle properties. Part I: Scheme description and idealized tests.

446   Journal of the Atmospheric Sciences, 72, 287–311. https://doi.org/10.1175/JAS-D-14-

447   0065.1

448   Muller, C. J., & Held, I. M. (2012). Detailed Investigation of the Self-Aggregation of

449   Convection in Cloud-Resolving Simulations, Journal of the Atmospheric Sciences,

450   69(8), 2551-2565. https://doi.org/10.1175/JAS-D-11-0257.1

451   Nakajima, K., & Matsuno, T. (1988). Numerical experiments concerning the origin of cloud

452   clusters in the tropical atmosphere. Journal of the Meteorological Society of Japan, 66,

453   309-329. https://doi.org/10.2151/jmsj.81.713

454   Nishizawa, S., Yashiro, H., Sato, Y., Miyamoto, Y., & Tomita, H. (2015). Influence of grid

455   aspect ratio on planetary boundary layer turbulence in large-eddy simulations.

456   Geoscientific Model Development, 8(10), 3393–3419. https://doi.org/10.5194/gmd-8-

457   3393-2015

458   Nishizawa, S., & Kitamura, Y. (2018). A surface flux scheme based on the Monin-Obukhov

459   similarity for finite volume models. Journal of Advances in Modeling Earth Systems,

460   10, 3159– 3175. https://doi.org/10.1029/2018MS001534

461   Pauluis, O., & Mrowiec, A. A. (2013). Isentropic analysis of convective motions. Journal of

462   the Atmospheric Sciences, 70, 3673–3688. https://doi.org/10.1175/JAS-D-12-0205.1

463   Pauluis, O. (2016). The mean air flow as Lagrangian dynamics approximation and its

464   application to moist convection. Journal of the Atmospheric Sciences, 73, 4407–4425.

465   https://doi.org/10.1175/JAS-D-15-0284.1

466   Sato, Y., Nishizawa, S., Yashiro, H., Miyamoto, Y., Kajikawa, Y., & Tomita, H. (2015).

467   Impacts of cloud microphysics on trade wind cumulus: Which cloud microphysics

468   processes contribute to the diversity in a large eddy simulation? Progress in Earth and

469   Planetary Science, 2(1), 23. https://doi.org/10.1186/s40645-015-0053-6

470   Sato, Y., Shima, S., & Tomita, H. (2018). Numerical convergence of shallow convection cloud

471   field simulations: Comparison between double-moment Eulerian and particle-based

472   Lagrangian microphysics coupled to the same dynamical core. Journal of Advances in

473   Modeling Earth Systems, 10, 1495– 1512. https://doi.org/10.1029/2018MS001285

474   Scotti, A., Meneveau, C., & Lilly, D. K. (1993). Generalized Smagorinsky model for

475   anisotropic grids. Physics of Fluids A: Fluid Dynamics, 5(9), 2306–2308.

476   https://doi.org/10.1063/1.858537

477   Sekiguchi, M., & Nakajima, T. (2008). A k-distribution-based radiation code and its

478   computational optimization for an atmospheric general circulation model. Journal of

479   Quantitative Spectroscopy and Radiative Transfer, 109(17–18), 2779–2793.

480   https://doi.org/10.1016/j.jqsrt.2008.07.013

481   Su, C.-Y., Wu, C.-M., & Chen, W.-T. (2019). Object-based precipitation system bias in grey

482   zone simulation: the 2016 South China Sea summer monsoon onset. Climate Dynamics,

483   53, 617–630. https://doi.org/10.1007/s00382-018-04607-x

484   Tanji, S., & Inatsu, M. (2019). Case study of blowing snow potential diagnosis with dynamical
485   downscaling. Scientific Online Letters on the Atmosphere, 15, 32-36,
486   https://doi.org/10.2151/sola.2019-007

487   Tomita, H. (2008). New microphysical schemes with five and six categories by diagnostic
488   generation of cloud ice. Journal of the Meteorological Society of Japan, 86A, 121–142.
489   https://doi.org/10.2151/jmsj.86A.121

490   Tompkins, A. M., & Craig, G. C. (1998). Radiative-convective equilibrium in a three-
491   dimensional cloud-ensemble model. Quarterly Journal of the Royal Meteorological
492   Society, 124, 2073–2097. https://doi.org/10.1002/qj.49712455013

493   Tsai, J.-Y., & Wu, C.-M. (2016). Critical transitions of stratocumulus dynamical systems due
494   to perturbation in free atmosphere moisture. Dynamics of Atmospheres and Oceans, 76,
495   1–13. https://doi.org/10.1016/j.dynatmoce.2016.08.002

496   Tsai, W.-M., & Wu, C.-M. (2017). The environment of aggregated deep convection. Journal
497   of Advances in Modeling Earth Systems, 9, 2061–2078,
498   https://doi.org/10.1002/2017MS000967.

499   Wilson, K. D. (2001). An alternative function for the wind and temperature gradients in
500   unstable surface layers. Boundary-Layer Meteorology, 99(1), 151–158.
501   https://doi.org/10.1023/A:1018718707419

502   Wing, A. A., & Emanuel, K. (2014). Physical mechanisms controlling self-aggregation of
503   convection in idealized numerical modeling simulations. Journal of Advances in
504   Modeling Earth Systems, 6, 59–74. https://doi.org/10.1002/2013MS000269

505   Wing, A. A., Reed, K. A., Satoh, M., Stevens, B., Bony, S., & Ohno, T. (2018). Radiative-
506   Convective Equilibrium Model Intercomparison Project. Geoscientific Model
507   Development, 11, 793–813. https://doi.org/10.5194/gmd-11-793-2018

508   Wing, A. A., Stauffer, C. L., Becker, T., Reed, K. A., Ahn, M.-S., & Arnold, N. P., et al. (2020).

509   Clouds and convective self-aggregation in a multimodel ensemble of radiative-

510   convective equilibrium simulations. Journal of Advances in Modeling Earth Systems,

511   12(9), 1942-2466. https://doi.org/10.1029/2020MS002138

512   Wing, A.A. (2019). Self-aggregation of deep convection and its implications for climate.

513   Current Climate Change Reports, 5, 1–11. https://doi.org/10.1007/s40641-019-00120-

514   3

515   Wu, C.-M., & Arakawa, A. (2011). Inclusion of surface topography into the vector vorticity

516   equation model (VVM). Journal of Advances in Modeling Earth Systems, 3, M04002.

517   https://doi.org/10.1029/2011MS000061

518   Wu, C.-M., & Arakawa, A. (2014). A unified representation of deep moist convection in

519   numerical modeling of the atmosphere. Part II. Journal of the Atmospheric Sciences,

520   71(6), 2089–2103. https://doi.org/10.1175/JAS-D-13-0382.1

521   Wu, C.-M., & Chen, P.-Y. (2021). Idealized cloud-resolving simulations of land-atmosphere

522   coupling over tropical islands. Terrestrial, Atmospheric and Oceanic sciences journal,

523   in press. https://doi.org/ 10.3319/TAO.2020.12.16.01

524   Wu, C.-M., Lin, H.-C., Cheng, F.-Y., & Chien, M.-H. (2019). Implementation of the land

525   surface processes into a vector vorticity equation model (VVM) to study its impact on

526   afternoon thunderstorms over complex topography in Taiwan. Asia-Pacific Journal of

527   Atmospheric Sciences. https://doi.org/10.1007/s13143-019-00116-x

528   Yanase, T., & Takemi, T. (2018). Diurnal variation of simulated cumulus convection in

529   radiative-convective equilibrium. Scientific Online Letters on the Atmosphere, 14, 116-

530   120. https://doi.org/10.2151/sola.2018-020

531   Yanase, T., Nishizawa, S., Miura, H., Takemi, T., & Tomita, H. (2020). New critical length for

532   the onset of self-aggregation of moist convection. Geophysical Research Letters, 47,

533   e2020GL088763. https://doi.org/10.1029/2020GL088763

534